Computational Materials Science 130 (2017) 144–151

Contents lists available at ScienceDirect

Computational Materials Science

journal homepage: www.elsevier.com/locate/commatsci

Stress wave propagation in Boron-Nitride nanotubes

Puneet Kumar Patra *, Romesh C. Batra

Biomedical Engineering and Mechanics, M/C-0219, Virginia Polytechnic Institute and State University, Blacksburg, VA 24060, USA

ARTICLE INFO

Article history:
Received 3 September 2016
Received in revised form 24 December 2016
Accepted 6 January 2017

Keywords:
Boron nitride
Wave propagation
Fermi-Pasta-Ulam
Molecular dynamics

ABSTRACT

The propagation of axial stress waves in Boron-Nitride nanotubes of different chirality and length under adiabatic conditions has been studied using molecular dynamics (MD) simulations. The velocities of the axial stress waves are found using three methods - (i) direct MD simulations, (ii) harmonic approximation of the nanotubes, and (iii) one-dimensional (1-D) wave equation. The MD simulation results indicate a small dependence of the wave velocities on the nanotube chirality and the excitation frequency – in armchair and zigzag nanotubes waves travel faster than that in chiral nanotubes, and wave velocities decrease with an increase in the frequency of excitation. The wave speed obtained from the harmonic approximations is ≈ 20—25% higher than that found from the MD simulations. Likewise, the frequencies of vibrations from the two approaches differ by 15–20% for most of the cases. The computation of the wave speed from 1-D equation requires a prior knowledge of the elastic modulus and the nanotube wall thickness. The values of these parameters are found from MD simulation results – axial tensile tests provide an estimate of the wall thickness scaled elastic modulus and the transverse vibration data relates the standard deviation of the tip displacement with material properties of the nanotube. The wave speed predicted from the 1-D wave equation agrees with that obtained from the MD simulations at low excitation frequencies. The contribution of the anharmonicity to the dynamics during wave propagation is found by matching the response of the anharmonic Fermi-Pasta-Ulam chain with the MD simulation results.

1. Introduction

The discovery of nanotubes, both Boron-Nitride (BNNT) and Carbon (CNT), has been one of the most promising findings in nanotechnology. These nanotubes possess exceptional specific mechanical strength [1,2], chemical properties [3], thermal stability [4] and electronic properties [5]. Experimental investigations with electric field induced resonance [6], X-ray scattering measurements [7] and bending tests using high-resolution transmission electron microscope [8] have revealed that Young's modulus of a BNNT is ≈722 GPa to 1.22 TPa, orders of magnitude higher than that of steel when the mass density is considered.

By using different analytical and simulation tools – classical molecular dynamics (MD) [9–13], ab initio [14] and tight-binding [15] MD, and first principles based study [16], it has been found that the elastic and the shear moduli of BNNTs depend upon their chirality and aspect ratio [17]. The chirality also significantly influences the torsional response of the nanotubes. The MD studies indicate that BNNTs are thermally stable up to ≈3700 K [9]. Thus BNNTs have been used in several interesting applications such as protective shields for nanomaterials [18], adsorption of gases [19], hydrogen storage [20], water purification [21] and nanomechanical sensors [22].

While the aforementioned computational methods are powerful, they require large computational resources. Researchers have, therefore, used structural mechanics and combined finite-element modeling to develop the atomic scale finite-element models (AFEM) [23,24]. Utilizing AFEM, Tao et al. [25] studied elastic properties of BNNTs, and evaluated buckling characteristics and Young's modulus by assuming the wall thickness of 0.34 nm. The stiffness matrix was formed by numerically displacing the atoms from their equilibrium positions. Similarly, Giannopoulos et al. [26,27] investigated the free vibration response of BNNTs and the tensile fracture behavior of Boron-Nitride nanoribbons along with the boundary conditions, the length and the diameter dependence of elastic properties, assuming the wall thickness to be 0.333 nm. Chowdhury et al. [28] used molecular mechanics (MM) simulations for finding optimized structures of BNNTs and their vibrational behaviors. Using the Euler-Bernoulli beam theory and MM, Chowdhury and Adhikari [29] modeled BNNT resonators. Jiang and Guo [30] developed an analytical model using MM to evaluate the size dependent elastic properties of BNNTs. The development of these models has enabled the bridging of scales through

* Corresponding author.
E-mail addresses: pkpatra@vt.edu (P.K. Patra), rbatra@vt.edu (R.C. Batra).

http://dx.doi.org/10.1016/j.commatsci.2017.01.008
0927-0256/

equivalent continuum structures (ECSs) [31]. However, the understanding of the BNNTs deformations significantly depends on the assumed material properties like the wall thickness and Poisson's ratio [28,32,33]. For example, the wall thickness of the nanotubes has been assumed to vary from 0.065 nm [33] to 0.34 nm [23]. Likewise, the Poisson's ratio varies from being negative [34] to positive [35]. It must be noted that MM and other related techniques do not account for thermal fluctuations present in the nanotube.

Bridging the nano- and the continuum scales in an ECS requires an in-depth analysis of differences in behaviors of the nano- and the continuum models. Here we focus on studying the propagation of axial stress waves in BNNTs. While the propagation of thermal waves has been extensively studied [36,37], only a few studies exist regarding the propagation of stress waves in BNNTs. Stress waves have been found to fracture nanotubes under excessive tensile loadings upon the release of the accumulated elastic energy [38]. In this work, the stress wave propagation results from MD simulations are compared with those obtained from the harmonic approximations (HAs). The method of obtaining the HA equivalent structure is similar to that of the AFEM from the MM. Specifically, the speed of the axial stress waves and the frequencies of vibration are compared to assess the suitability of the HAs in solving nanoscale problems. While the wave speeds through MD simulations show frequency dependence, they are frequency-independent from the HAs. Additionally, the wave speeds and frequencies are found to vary by 15–25%. The contribution of the anharmonicity to the dynamics is ≈20%, obtained by matching the response of an anharmonic Fermi-Pasta-Ulam chain with that from the MD simulations. Results of transverse vibrations and axial tensile tests are utilized to find the wall thickness and the elastic modulus of the BNNTs by handshaking MD results with the vibration properties of a beam. Using these thickness and elastic modulus values, the wave speed obtained from the continuum 1-D wave equation is found to agree well with that from the MD simulations at low excitation frequencies.

2. Simulations and analysis

2.1. Modeling the system

A BNNT may be imagined to be obtained by rolling a hexagonal Boron-Nitride sheet comprised of hexagonal rings in which every Boron atom is covalently bonded to three other Nitrogen atoms (and vice versa), with the nearest BN bond length, $a = 1.4457$ Å [39]. A typical BNNT is characterized by three parameters - the length (l), and the chiral indices (n, m) that determine the rolling direction of the hexagonal sheet. The diameter, D, and the chiral angle, θ, of a nanotube in terms of the chiral indices are given by:

$$D = \frac{a}{\pi} \times \sqrt{3(m^2 + mn + n^2)} \tag{1}$$

$$\theta = \tan^{-1}\left(\frac{\sqrt{3}m}{2n + m}\right) \tag{2}$$

Depending upon values of m and n, one gets three different types of nanotubes: (i) $m = n$ gives an armchair nanotube, (ii) $m = 0, n > 0$ gives a zigzag nanotube, and (iii) $0 < m < n$ gives a chiral nanotube. It is evident that the chiral angle θ is in the range $[0, 30^\circ]$. Nanotubes of 4 different chiralities: $(10,10), (12,8), (15,4)$ and $(17,0)$, and three different lengths, $l = 70$ nm,140 nm and 210 nm, have been investigated in this study. The nanotubes have been chosen such that each has $D \approx 1.38$ nm. The three different lengths help us identify essential features of the stress wave propagation, and the interaction between the incident and the reflected waves. The atoms of an BNNT interact with each other through the three-body Tersoff type potential [40]. Details of the potential function are given in Ref. [41]. Several different Tersoff parameters have been proposed for the Boron-Nitride interactions. Here, values of parameters given by Sevik et al. [41] that have been shown to provide good agreement between experimental and computational results are used.

All MD simulations have been performed by using the open-source software, LAMMPS [42]. The simulation begins with a conjugate gradient energy minimization. The simulation domain is then divided into three regions along the axial (z) direction - the 1 nm long leftmost region, the 1 nm long rightmost region, and the middle region comprised of the rest of the nanotube. Only the rightmost region is kept fixed for the remainder of the simulations. Subsequently, the MD simulations are conducted at the constant temperature of 0.01 K using the Langevin thermostat for 40,000 time steps with an integration time-step of 1.0 fs.

2.2. Computing wave speeds from MD simulations

A stress wave is imposed on the nanotube by axially displacing atoms of the leftmost region in a sinusoidal manner:

$$z(t) = z(0) + 0.5 \sin\left(\omega_f t\right), \tag{3}$$

and the frequency ω_f is varied systematically from 0.5 THz to 5 THz in 10 simulation runs. The boundary conditions imposed at the two end faces of the BNNT are shown in Fig. 1. While atoms on the rightmost boundary are kept fixed, those on the leftmost boundary are allowed to move only in the axial direction. As mentioned above, atoms in the middle region are un-constrained. Furthermore, the Langevin thermostat is removed and simulations are performed at a constant energy ensemble.

The displacement is imposed for 600,000 time steps where each integration time step equals 0.1 fs. In order to compute the wave speeds, we find the distance through which the first peak of the wave propagates since the beginning of the simulation by closely studying snapshots of the wave at 10 different times. If the distance travelled by the wave in time t_k is d_k, then the average wave speed is computed as:

$$\langle c \rangle = \frac{\sum_{k=2}^{10} \frac{d(t_k) - d(t_1)}{t_k - t_1}}{9}. \tag{4}$$

The entire procedure is shown in Fig. 2. Alternatively, the speed may be obtained from the time at which the wave crosses a fixed location of the nanotube [43].

2.3. Wave speed using the harmonic approximations

At very low temperatures, the dynamics of the nanotubes is harmonic [44]. We thus numerically compute the Hessian matrix. As schematically shown in Fig. 3, for the post minimization and equilibration runs, each ring of a nanotube is treated as a single particle with its z-coordinate equal to the axial location of the ring. The boundary conditions considered are the same as those shown in Fig. 1. The distance between two adjacent particles is ≈ 0.125 nm. Thus, for a 70 nm long nanotube there are 560 particles. A particle is first displaced by $\Delta = 0.001$ nm in the positive z direction, and forces on all particles are computed. Similarly, the particle is displaced by $-\Delta$ along the z direction and the resulting forces are obtained. Stiffness terms are then computed using the relation:

$$K_{ij} = -\frac{F_{ij}(\Delta) - F_{ij}(-\Delta)}{2\Delta}, \tag{5}$$

where F_{ij} denotes the force on the equivalent particle j when the particle i is displaced. To ensure real eigenvalues, the matrix $[K]$ is

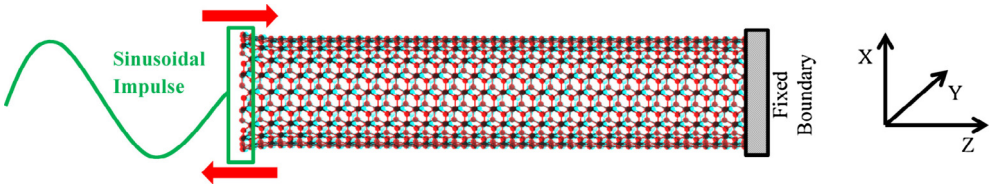

Fig. 1. Boundary conditions imposed for studying the axial stress wave propagation: atoms on the rightmost boundary are kept fixed, atoms of the leftmost boundary are axially displaced in a sinusoidal manner, and those in the middle region evolve without applying any constraints.

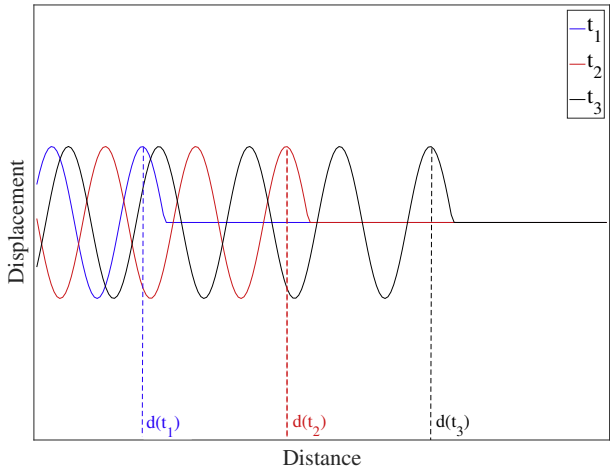

Fig. 2. Determination of the wave speed from MD simulations. The figure shows the snapshot of a traveling wave at three different times (t_1, t_2, t_3). The distance, $(d(t_1), d(t_2), d(t_3))$, travelled by the first peak of the wave is determined at the three times. For simplicity snapshots at only three time are shown. In actual evaluation, 10 such time snapshots are used, and the speed is calculated from Eq. (4).

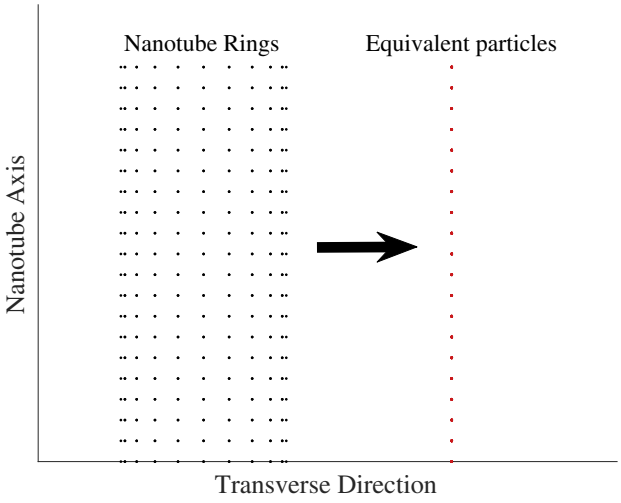

Fig. 3. For determining the stiffness elements of the nanotube along the axial direction, each nanotube ring (black dots) is represented by an equivalent particle (red dots). Each equivalent particle is then displaced from its equilibrium position by $\pm\Delta$, and the forces on all particles are computed. Elements of the stiffness matrix are determined using the central-difference method. (For interpretation of the references to color in this figure legend, the reader is referred to the web version of this article.)

symmetrized. The forced vibration response of the equivalent particle-based structure is governed by the equation:

$$[M]\{\ddot{z}\} + [K]\{z\} = F, \tag{6}$$

where $[M]$ is a diagonal matrix denoting the mass of each equivalent particle and F is the forcing vector whose only nonzero element is the first element: $F_1 = 1.0\sin(\omega_f t)$. As before, ω_f varies from 0.5 to 5 THz. The coupled equations of motion are decoupled by using the normal modal analysis [45]. The steady state system response is given by:

$$\{z_i(t)\} = \sum_{j=1}^{N} \frac{\Phi_j \Phi_j^T F_i(t)}{M_{jj}(\omega_j^2 - \omega_f^2)}, \tag{7}$$

where Φ_j is the jth eigenvector corresponding to the jth natural frequency ω_j. The steady-state solution corresponds to standing waves with the distance between two consecutive nodes equalling $\lambda/2$. The wave speed is then determined using:

$$c = \frac{\omega_f}{\lambda}, \tag{8}$$

2.4. Contribution of anharmonicity

During the MD simulations the temperature of the system rises because of the continuous work added due to the displacement imposed on atoms at the left edge. Thus anharmonic effects may influence the system dynamics. In order to quantify the effects of anharmonicity, we consider the Fermi-Pasta-Ulam [46,47] chain comprised of N spring mass systems and the Hamiltonian:

$$H = \sum_{n=1}^{N} \frac{p_n^2}{2m_c} + \sum_{n=1}^{N} \frac{1}{2} k_1 (z_{n+1} - z_n - d_0)^2 + \sum_{n=1}^{N} \frac{1}{4} k_2 (z_{n+1} - z_n - d_{eq})^4. \tag{9}$$

The chain consists of N particles each interacting with its nearest neighbors by a harmonic potential (second term in Eq. (9)) and a tethering anharmonic potential (the third term in Eq. (9)). Here, p_n and z_n denote the momentum and the position of the nth particle, respectively. Equilibrium position of the nth particle is given by its initial z-coordinate ($= n$). For simplicity we assume that each particle is of mass m_c. The equilibrium distance between two adjacent particles is given by d_{eq}, and k_1 and k_2 denote, respectively, strengths of the harmonic and the anharmonic potentials. Here we take $m_c = 1$, $d_{eq} = 1$. The rightmost particle is kept fixed while the leftmost particle is given a forced sinusoidal displacement similar to that deduced from Eq. (3). Because of the forced vibration, a standing wave forms within the chain. The value of k_2 is iterated upon to get a response resembling the standing wave patterns obtained from the MD simulations. The equations of motion derived from Eq. (9) are solved using the 4th order Runge-Kutta algorithm with an incremental time step of 10^{-5} for a total of 10^7 time steps.

2.5. Evaluation of wall-thickness

The evaluation of the wall-thickness requires proper handshaking between the continuum and the atomic scales using the

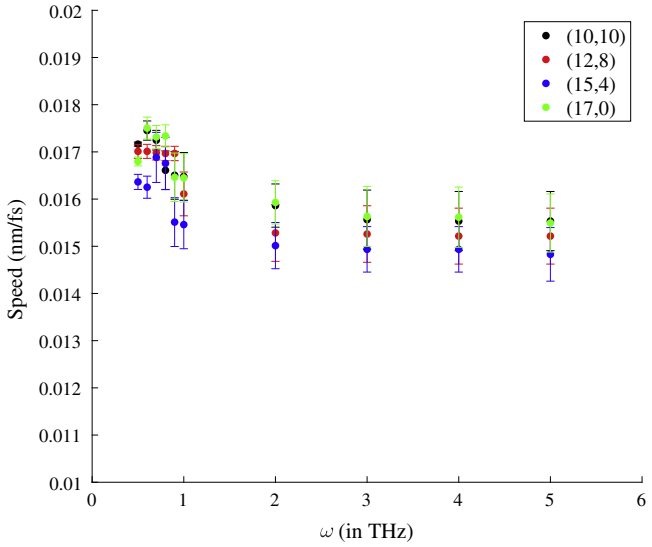

Fig. 4. The average speed and the error bars of the axial stress waves (in nm/fs) for the four BNNTs. There is a marginal dependence of wave speeds on both the circular excitation frequency and the tube chirality. With increasing ω wave speeds reach a saturated value. The wave speed is higher in the zigzag and the armchair nanotubes than that in the chiral nanotubes.

approach of Refs. [48,49]. Assuming that the nanotube with the boundary conditions shown in Fig. 1 can be modeled as an equivalent cantilever beam, the tip vibration of the nanotube from statistical mechanical theory is correlated with that from the MD simulations. For evaluating the wall-thickness of the nanotube, natural (free) vibrations are sufficient. Since the free vibration response is dominated by the transverse displacement, the tip vibration (or bending vibrations) in the lateral direction is considered.

Referring the reader to Krishnan et al. [49] for the detailed derivation, the solution of the transverse vibration equation of the beam is used to deduce the natural frequencies, ω_j, and the corresponding modal elastic energy. For the tip displacement, $y(t)$, at a particular time, and the beam vibrating at the natural frequency ω_j, the conditional distribution function of $y(t), f(y(t)|\omega_j)$, is obtained. Statistical mechanics is then invoked to find the probability density of the system to vibrate at ω_j. Lastly the marginal probability density of y is obtained by the convolution: $f(y) = \int f(y(t)|\omega_j) f(\omega_j) d\omega_j$. It is found that the probability density function of the tip vibration is normally distributed. Thus, the variance of y can be related to the standard deviation of the distribution function by:

$$\langle y^2 \rangle = \frac{0.8488 l^3 k_B T}{EqD^3(1 + (q/D)^2)}, \tag{10}$$

where E is the elastic modulus, q the wall thickness of the nanotube, D the tube mean-diameter, k_B the Boltzmann constant, and T the temperature of the system. Since two unknowns (E, q) are present in Eq. (10), another equation is needed for obtaining q. This is derived by performing a separate set of simulations involving uniaxial tensile extension of the nanotubes. The change in the elastic energy, U, due to the applied loading can be related to E and q through:

$$Eq = \frac{1}{\pi D l} \frac{\partial^2 U}{\partial \epsilon^2}, \tag{11}$$

where ϵ represents the axial strain, and q is assumed to be much smaller than D.

We now describe the two simulation strategies employed for computing q from Eqs. (10) and (11). The convergence of $\langle y^2 \rangle$ requires analyzing the nanotube dynamics for a long time-duration. In order to keep the CPU time reasonable, the tube length l is shortened to 20 nm for this set of simulations. A constant temperature environment of 100 K is imposed by using the Langevin thermostat for post-equilibration (see Section 2.1) simulations. Each nanotube ring is considered as an equivalent single beam particle (similar to that shown in Fig. 3) and the transverse displacement of the free end is found. A separate set of simulations is carried out with the free end of the nanotube displaced axially at the rate of 0.001 nm/fs. The change in the potential energy of the system is monitored, and Eq. (11) is used to find $E \times q$, which is then substituted in Eq. (10) to deduce the value of the wall-thickness q.

Other approaches for finding the nanotube wall thickness from MM simulations are described in Refs. [50–52].

3. Results and discussion

The CPU time for a simulation is 1–3 h (depending upon the nanotube length) with 8 processors [Intel(R) Xeon(R) E5420@2.50 GHz] used concurrently. As is typical of an MD simulation, most of the computational time is spent in evaluating the forces ($\approx$ 90–95%).

3.1. Wave speed in different nanotubes from MD simulations

The methodology described in Section 2.2 is used to obtain the wave speeds from MD simulations and the results are depicted in Fig. 4. The speed of the axial stress wave is found to marginally depend upon the nanotube chirality and the excitation frequency. For nearly all cases, the zigzag (17,0) nanotube has the maximum wave speed. This is followed by that of the armchair (10,10) nanotube, and the waves travel the slowest in the chiral nanotubes. Except for the (17,0) nanotube, the maximum wave speed is obtained at $\omega = 0.6$ THz. The ratio of the maximum wave speed to the minimum wave speed varies between 1.12 and this agrees with that obtained from the phonon-dispersion relationship for acoustic modes where the wave velocity decreases at large ω.

Table 1
Speed of waves (in nm/fs) for different frequencies obtained from the harmonic approximation. The speed has a marginal dependence on the nanotube chirality, but is independent of the excitation frequency. The wave speed decreases with an increase in the chiral angle unlike the results from the MD simulations that give the opposite trend.

	$\langle c \rangle$ for different chiralities			
ω_f (in THz)	(10,10)	(12,8)	(15,4)	(17,0)
1	0.0203	0.0203	0.0212	0.0218
2	0.0202	0.0210	0.0210	0.0218
3	0.0204	0.0209	0.0213	0.0220
4	0.0204	0.0207	0.0212	0.0218
5	0.0203	0.0205	0.0213	0.0217
Average	0.0203	0.0207	0.0212	0.0218

Table 2
Comparison of the first five natural frequencies (in THz) of the 70 nm long (10,10) armchair BNNT obtained from the MD and the HA approaches. The average difference in the results from the two approaches is 18%.

	ω_j (in THz) for different chiralities							
	(10,10)		(12,8)		(15,4)		(17,0)	
j	MD	HA	MD	HA	MD	HA	MD	HA
1	0.80	0.94	0.81	1.09	0.86	0.99	0.76	0.89
2	1.60	1.88	1.60	1.97	1.55	1.97	1.60	1.78
3	2.44	2.82	2.49	2.90	2.44	2.96	2.44	2.67
4	3.27	3.76	3.33	3.83	3.27	3.94	3.27	3.55
5	4.11	4.69	4.95	4.77	4.06	4.93	4.90	3.44

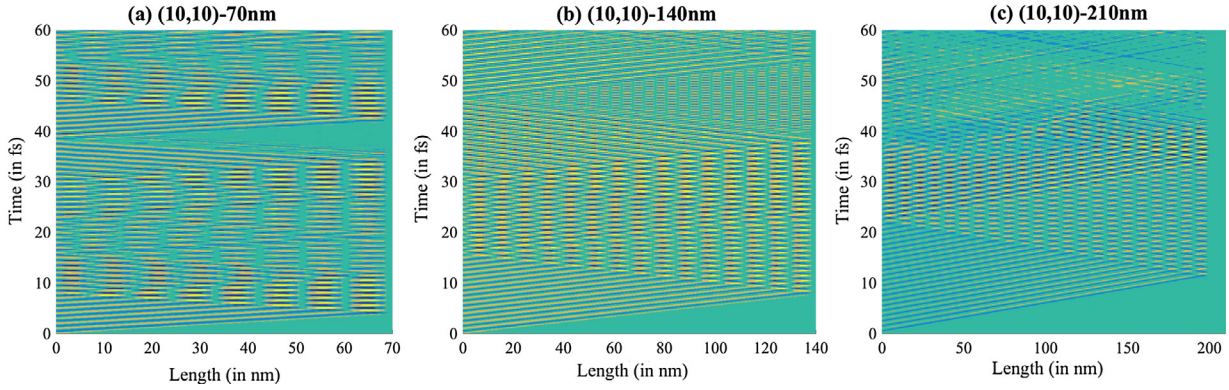

Fig. 5. Spatiotemporal plots of the velocity along the z-direction for the (10,10) armchair nanotube of three different lengths: (a) 70 nm, (b) 140 nm, and (c) 210 nm. The figures correspond to the constant energy ensemble. Notice different interaction patterns for the three tube lengths. The incident and the reflected waves interact to create constructive and destructive interference. The amplitude of the maxima/minima depends upon the nanotube length.

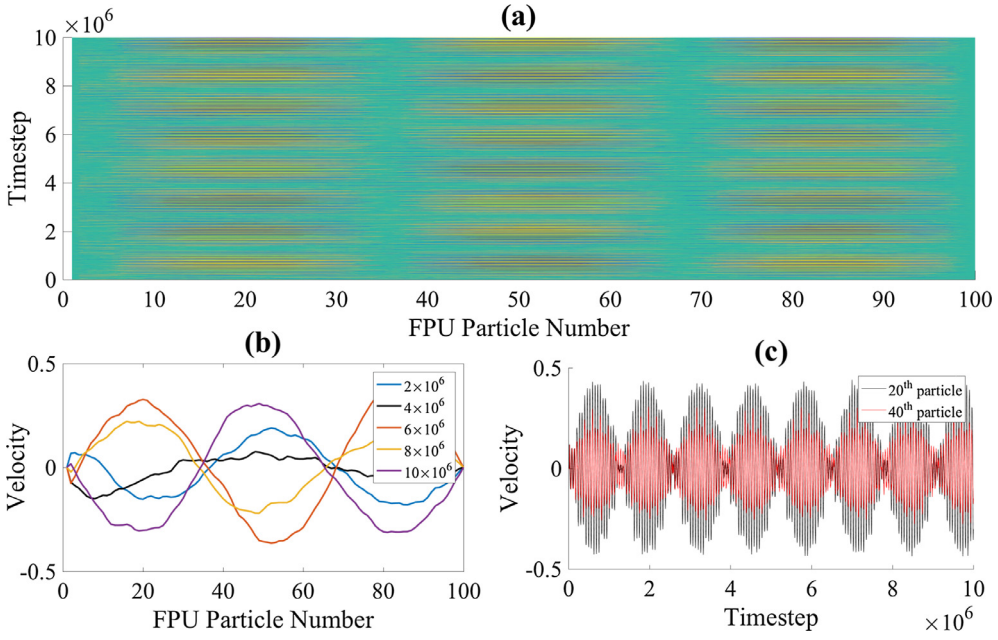

Fig. 6. (a) Spatiotemporal plot of the velocity for a purely harmonic $N = 100$ particle FPU chain, (b) snapshots of the velocity profile at 5 different times, and (c) temporal history of the axial velocity for the 20th and the 40th particles. Notice the difference between the results depicted in this figure (a) and the spatiotemporal plots shown in Fig. 5. Here, the nodes and the antinodes persist throughout the simulation. The small error in locating the position of the nodes (see (b)) is due to the numerical approach. The standing wave formed in the chain is comprised of at least two different frequencies, as is evident from the results exhibited in (c).

3.2. Wave speed from harmonic approximation analysis

Using the approach described in Section 2.3, the wave speeds found for the different BNNTs are listed in Table 1. The wave propagation is found to be independent of the excitation frequency, but depends marginally on the tube chirality. Unlike the MD simulation results for which the armchair and the zigzag nanotubes gave the fastest wave speeds, here the wave propagation is the slowest for the armchair nanotube. With increasing chiral angle, the wave speed decreases. The difference between the wave speeds from the MD and the HAs varies from 20 to 25%.

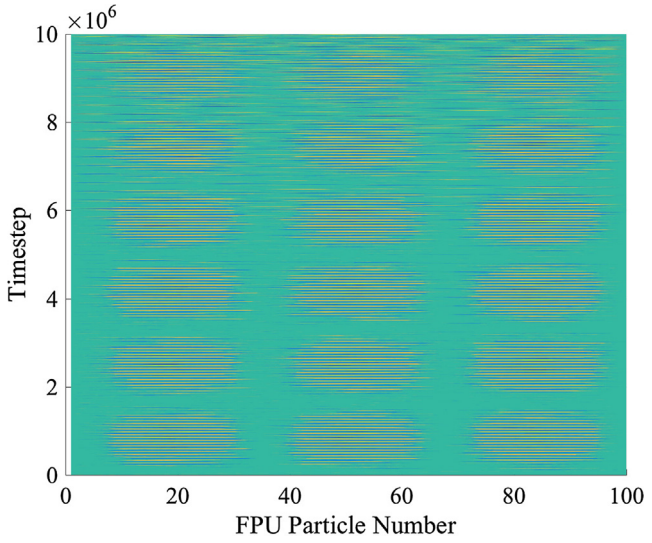

Fig. 7. Spatiotemporal plot of the velocity for $N = 100$ particle FPU chain with $k_2 = 0.20$. The value of k_2 is incremented in steps of 0.01 until nodes of the standing waves disappear. The figure is reminiscent of the spatiotemporal plot of the (10,10) nanotube shown in Fig. 5(c). The results indicate that the anharmonic effects contribute $\approx 20\%$ to the system dynamics.

3.3. Continuous wave propagation

Nanotubes are divided into 200 distinct non-overlapping strips for calculating different parameters. Each strip comprises of several particles, and the results presented are their mean values. The atomic counterpart of the continuum Cauchy stress is the Virial stress, defined as:

$$\sigma_{\gamma\delta} = \frac{1}{V}\sum_{\alpha}\left[r_{\gamma}^{\alpha}F_{\gamma}^{\alpha} - m^{\alpha}v_{\gamma}^{\alpha}v_{\delta}^{\alpha}\right] \tag{12}$$

Here (γ, δ) take values of the x, y and z directions, F^{α} denotes the total force on the particle α having a position vector $\mathbf{r}^{\alpha}$, and V denotes the volume of the system. The computation of the Virial stresses for a nanotube is nontrivial due to the ill-defined nature of the volume of the system. For the present problem, since the system has been equilibrated at 0.01 K, the initial contribution of the velocity terms in Eq. (12) to the Virial stress is considered negligible. Subsequently, since the nanotubes undergo NVE dynamics (free of any thermostat influence), the axial component of the particle velocity is used as a proxy for the propagation of stress waves without computing the Virial stress. However, this approximation will not be valid when the particle dynamics is under a constant temperature environment.

The natural frequencies of vibration are derived from the MD simulations by taking the Fourier transform of the velocity autocorrelation function. Only the axial velocity component is considered. These natural frequencies are compared with those obtained from the harmonic approximation approach. Results given in Table 2 indicate that frequencies from the two analyses differ by 15–20% and by 30% for the 5th mode of the (17,0) nanotube.

We now discuss results of a wave train propagating in the nanotube. From the fixed right end the compressive axial wave is reflected as a tensile axial wave of twice the amplitude. As expected, the axial velocity of the particles remains close to zero prior to the passage of the stress wave. Until the incident and the reflected waves interact, the velocity profile at a cross-section resembles that of the incident wave-velocity. The incident and the reflected waves interact with each other to form standing waves with nodes and antinodes. The standing waves for the (10,10) nanotubes are shown in Fig. 5. The plots illuminate how the disturbance due to the sinusoidal loading propagates along the nanotube spatially as well as temporally. A section perpendicular to the tube axis provides the temporal evolution of the axial velocity at a particular cross-section of the nanotube. Likewise, a section perpendicular to the time axis provides the time snapshot of the axial velocity profile of the nanotube. Green regions between two subsequent yellow and blue[1] regions have zero axial velocity, denoting the presence of nodes. However, if the wave propagation is studied for longer durations, the nodes and the antinodes become less prominent, especially for the longer nanotubes. It is interesting to note that the kinetic energy due to the motion along the transverse direction keeps on increasing with time. This may be attributed to the nature of the potential of the system since it has coupling among different degrees of freedom. These results may be viewed as an approach towards equilibration by the nanotubes.

These results are in sharp contrast to those for typical wave propagation observed in one-dimensional (1-D) systems like elastic bars or stretched strings. In order to better elucidate the differences, we first consider a purely harmonic 1-D chain ($k_2 = 0$ in Eq. (9)) with $N = 100$. The equations of motion are solved for 1×10^7 time steps. The free end of the chain is subjected to a sinusoidal displacement of amplitude 1.0 and $\omega = 0.1$. The results displayed in Fig. 6(a), (b), and (c), respectively, show the entire spatiotemporal evolution of velocity along the chain as the wave propagates, the spatial profile of the axial velocity at five distinct time-steps, and the temporal history of the velocity of two particular particles. Unlike for the results plotted in Fig. 5, the nodes and the antinodes persist throughout the simulation in this case. A small error is present in finding the exact location of the nodes and the antinodes owing to the finite length of the chain and the numerical integration of the governing equations. The chain vibrates in at least two different frequencies, as can be seen from Fig. 6(c).

We now add anharmonicity to the chain motion by increasing the value of k_2 in Eq. (9) in increments of 0.01 till the velocity profile similar to that in Fig. 5(c) is obtained. With $k_2 = 0.20$, a situation similar to that in Fig. 5(c) arises, as shown in Fig. 7. These results indicate that the anharmonic effects of the potential contribute $\approx 20\%$ towards the dynamics at long time.

3.4. Thickness determination

In this section, the wall-thickness of a nanotube is determined using the methodology discussed in Section 2.5. The values of thickness scaled elastic modulus, $E \times q$, and the wall-thickness, q, of the nanotubes so found are listed in Table 3. The computed wall-thickness varies from 0.295 nm to 0.365 nm, with an average value of 0.342 nm. This variation can be attributed to the possible non-convergence of $\langle y^2 \rangle$ in the simulation time duration. We note that the computation of the standard deviation requires a longer time for convergence in comparison to that of the mean values. One can use the values listed in Table 3 to evaluate E in typical stress units.

The stress-wave problem studied for the nanotubes may be modeled as a continuum scale 1-D wave equation:

$$\frac{\partial^2 u}{\partial t^2} = \frac{E}{\rho}\frac{\partial^2 u}{\partial z^2}. \tag{13}$$

Here u represents the displacement along the z-direction, E the elastic modulus, t the time and ρ the mass density. The speed of the wave is given by:

[1] For interpretation of color in Fig. 5, the reader is referred to the web version of this article.

Table 3
Scaled elastic modulus ($E \times q$) and q as determined from the methodology described in Section 2.5. The temperature used for the calculation was the average values during the simulation, and not the thermostatted temperature used for the initial equilibration. We believe that the wall-thickness for the different cases would approach the same value if simulations were performed for longer time durations.

	Chirality			
	(10,10)	(12,8)	(15,4)	(17,0)
$E \times q$ (in TPa nm)	0.2192	0.2341	0.2226	0.206
q (in nm)	0.344	0.364	0.365	0.295

$$c = \sqrt{\frac{E}{\rho}} \tag{14}$$

Based upon the length, the diameter and the mass of the atoms, one can determine the mass per unit area of the nanotube as $\approx 7.6 \times 10^{-7}$ kg/m^2. Using the values of E and q listed in Table 3, the wave speed (in nm/fs) from Eq. (14) equals 0.0169, 0.0174, 0.0170 and 0.0164, respectively, for the (10,10), (12,8), (15,4) and (17,0) BNNTs. These values agree with those obtained from the MD simulations at large excitation frequencies where little scattering is expected.

4. Conclusions

We have studied the axial wave propagation in Boron-Nitride nanotubes, and utilized the vibration data to obtain their elastic modulus and wall-thickness. The main conclusions drawn from the present study are summarized below.

1. The wave speed is the highest for a zigzag nanotube followed by that in an armchair and a chiral nanotube in MD simulations.
2. The wave speed decreases by a factor of 1.12–1.14 as the excitation frequency is increased from 0.5 to 5 THz.
3. The wave speed from the harmonic approximations is almost 25% greater than that from the MD simulations. Unlike in the MD simulations, waves travel faster in chiral nanotubes than in armchair nanotubes.
4. There is $\approx 18\%$ discrepancy between the frequencies of vibration derived from the MD and the harmonic approximation results.
5. When the nanotube is subjected to a wave train, waves reflected from the fixed end interact with the incident waves to create patterns resembling a standing wave. However, for a long nanotube after sufficiently large time duration, the nodes are not prominent.
6. By comparing the spatiotemporal wave pattern of velocities between the MD and an FPU chain results, it is found that the anharmonicity contributes $\approx 20\%$ to the tube dynamics.
7. The wall-thickness of the nanotubes is found to vary between 0.295 and 0.365 nm, and this variation may be reduced by calculating $\langle y^2 \rangle$ for longer time durations but has not been done here.
8. From the values of $E \times q$ and q, the wave speed determined using the 1-D continuum wave equation agrees with that obtained from the MD simulations for low excitation frequencies.

Acknowledgements

Authors are indebted to the reviewers for providing constructive comments on an earlier version of the manuscript that have helped improve upon the presentation of the work.

References

[1] J. Garel, I. Leven, C. Zhi, K.S. Nagapriya, R. Popovitz-Biro, D. Golberg, Y. Bando, O. Hod, E. Joselevich, Ultrahigh torsional stiffness and strength of boron nitride nanotubes, Nano Lett. 12 (12) (2012) 6347–6352.
[2] M. Santosh, P.K. Maiti, A.K. Sood, Elastic properties of boron nitride nanotubes and their comparison with carbon nanotubes, J. Nanosci. Nanotechnol. 9 (9) (2009) 5425–5430.
[3] D. Golberg, Y. Bando, C. Tang, C. Zhi, Boron nitride nanotubes, Adv. Mater. 19 (18) (2007) 2413–2432.
[4] W.-Q. Han, W. Mickelson, J. Cumings, A. Zettl, Transformation of BxCyNz nanotubes to pure BN nanotubes, Appl. Phys. Lett. 81 (6) (2002) 1110–1112.
[5] Z. Zhang, W. Guo, Y. Dai, Stability and electronic properties of small boron nitride nanotubes, J. Appl. Phys. 105 (8) (2009) 084312.
[6] A.P. Suryavanshi, M.-F. Yu, J. Wen, C. Tang, Y. Bando, Elastic modulus and resonance behavior of boron nitride nanotubes, Appl. Phys. Lett. 84 (14) (2004) 2527–2529.
[7] A. Bosak, J. Serrano, M. Krisch, K. Watanabe, T. Taniguchi, H. Kanda, Elasticity of hexagonal boron nitride: inelastic X-ray scattering measurements, Phys. Rev. B 73 (4) (2006) 041402.
[8] A. Raul, W. Ming-Sheng, X. Zhi, L. Annick, G. Dmitri, Young modulus, mechanical and electrical properties of isolated individual and bundled single-walled boron nitride nanotubes, Nanotechnology 22 (26) (2011) 265704.
[9] M. Won Ha, H. Ho Jung, Molecular-dynamics simulation of structure and thermal behaviour of boron nitride nanotubes, Nanotechnology 15 (5) (2004) 431.
[10] V. Veena, V.K. Jindal, D. Keya, Elastic moduli of a boron nitride nanotube, Nanotechnology 18 (43) (2007) 435711.
[11] M.-L. Liao, Y.-C. Wang, S.-P. Ju, T.-W. Lien, L.-F. Huang, Deformation behaviors of an armchair boron-nitride nanotube under axial tensile strains, J. Appl. Phys. 110 (5) (2011) 054310.
[12] A. Chandra, P.K. Patra, B. Bhattacharya, Thermal vibration characteristics of armchair boron-nitride nanotubes, J. Appl. Phys. 118 (23) (2015) 234503.
[13] C. Anirban, P. Puneet Kumar, B. Baidurya, Thermomechanical buckling of boron nitride nanotubes using molecular dynamics, Mater. Res. Express 3 (2) (2016) 025005.
[14] K.N. Kudin, G.E. Scuseria, B.I. Yakobson, c_2F, BN, and C nanoshell elasticity from ab initio computations, Phys. Rev. B 64 (23) (2001) 235406, pRB.
[15] H.F. Bettinger, T. Dumitric, G.E. Scuseria, B.I. Yakobson, Mechanically induced defects and strength of BN nanotubes, Phys. Rev. B 65 (4) (2002) 041406, pRB.
[16] D. Vahedi Fakhrabad, N. Shahtahmassebi, First-principles calculations of the Young's modulus of double wall boron-nitride nanotubes, Mater. Chem. Phys. 138 (23) (2013) 963–966.
[17] N.M. Anoop Krishnan, D. Ghosh, Chirality dependent elastic properties of single-walled boron nitride nanotubes under uniaxial and torsional loading, J. Appl. Phys. 115 (6) (2014) 064303.
[18] Y. Li, P.S. Dorozhkin, Y. Bando, D. Golberg, Controllable modification of sic nanowires encapsulated in BN nanotubes, Adv. Mater. 17 (5) (2005) 545–549.
[19] M.D. Ganji, A. Mirnejad, A. Najafi, Theoretical investigation of methane adsorption onto boron nitride and carbon nanotubes, Sci. Technol. Adv. Mater. 11 (4) (2010) 045001.
[20] X. Wu, J. Yang, J.G. Hou, Q. Zhu, Defects-enhanced dissociation of h2 on boron nitride nanotubes, J. Chem. Phys. 124 (5) (2006) 054706.
[21] W. Lei, D. Portehault, D. Liu, S. Qin, Y. Chen, Porous boron nitride nanosheets for effective water cleaning, Nat. Commun. 4 (2013) 1777.
[22] R. Chowdhury, S. Adhikari, Boron-nitride nanotubes as zeptogram-scale bionanosensors: theoretical investigations, IEEE Trans. Nanotechnol. 10 (4) (2011) 659–667.
[23] B. Liu, H. Jiang, Y. Huang, S. Qu, M.-F. Yu, K. Hwang, Atomic-scale finite element method in multiscale computation with applications to carbon nanotubes, Phys. Rev. B 72 (3) (2005) 035435.
[24] B. Liu, Y. Huang, H. Jiang, S. Qu, K. Hwang, The atomic-scale finite element method, Comput. Methods Appl. Mech. Eng. 193 (17) (2004) 1849–1864.
[25] J. Tao, G. Xu, Y. Sun, Elastic properties of boron-nitride nanotubes through an atomic simulation method, Math. Problems Eng. (2015).
[26] G.I. Giannopoulos, D.-P.N. Kontoni, S.K. Georgantzinos, Efficient FEM simulation of static and free vibration behavior of single walled boron nitride nanotubes, Superlattices Microstruct. 96 (2016) 111–120.
[27] G.I. Giannopoulos, S.K. Georgantzinos, Mechanical characterization of boron-nitride nanoribbons via nonlinear structural mechanics, Journal of Nano Research, vol. 40, Trans Tech Publ, 2016, pp. 58–71.

[28] R. Chowdhury, C. Wang, S. Adhikari, F. Scarpa, Vibration and symmetry-breaking of boron nitride nanotubes, Nanotechnology 21 (36) (2010) 365702.
[29] R. Chowdhury, S. Adhikari, Boron-nitride nanotubes as zeptogram-scale bionanosensors: theoretical investigations, IEEE Trans. Nanotechnol. 10 (4) (2011) 659–667, http://dx.doi.org/10.1109/TNANO.2010.2060492.
[30] L. Jiang, W. Guo, A molecular mechanics study on size-dependent elastic properties of single-walled boron nitride nanotubes, J. Mech. Phys. Solids 59 (6) (2011) 1204–1213, http://dx.doi.org/10.1016/j.jmps.2011.03.008. <http://www.sciencedirect.com/science/article/pii/S0022509611000536>.
[31] S.S. Gupta, P. Agrawal, R.C. Batra, Buckling of single-walled carbon nanotubes using two criteria, J. Appl. Phys. 119 (24) (2016) 245106.
[32] B. Mortazavi, Y. Rmond, Investigation of tensile response and thermal conductivity of boron-nitride nanosheets using molecular dynamics simulations, Physica E: Low-dimens. Syst. Nanostruct. 44 (9) (2012) 1846–1852.
[33] M.B. Panchal, S.H. Upadhyay, Cantilevered single walled boron nitride nanotube based nanomechanical resonators of zigzag and armchair forms, Physica E: Low-dimens. Syst. Nanostruct. 50 (2013) 73–82.
[34] L. Boldrin, F. Scarpa, R. Chowdhury, S. Adhikari, Effective mechanical properties of hexagonal boron nitride nanosheets, Nanotechnology 22 (50) (2011) 505702.
[35] M. Zheng, X. Chen, I.-T. Bae, C. Ke, C. Park, M.W. Smith, K. Jordan, Radial mechanical properties of single-walled boron nitride nanotubes, Small 8 (1) (2012) 116–121.
[36] J. Shiomi, S. Maruyama, Non-fourier heat conduction in a single-walled carbon nanotube: classical molecular dynamics simulations, Phys. Rev. B 73 (20) (2006) 205420.
[37] B. Li, J. Wang, L. Wang, G. Zhang, Anomalous heat conduction and anomalous diffusion in nonlinear lattices, single walled nanotubes, and billiard gas channels, Chaos 15 (1) (2005) 015121.
[38] T. Belytschko, S. Xiao, G.C. Schatz, R. Ruoff, Atomistic simulations of nanotube fracture, Phys. Rev. B 65 (23) (2002) 235430.
[39] A. Rubio, J.L. Corkill, M.L. Cohen, Theory of graphitic boron nitride nanotubes, Phys. Rev. B 49 (7) (1994) 5081–5084, pRB.
[40] J. Tersoff, Modeling solid-state chemistry: interatomic potentials for multicomponent systems, Phys. Rev. B 39 (8) (1989) 5566–5568, pRB.
[41] C. Sevik, A. Kinaci, J.B. Haskins, T. an, Characterization of thermal transport in low-dimensional boron nitride nanostructures, Phys. Rev. B 84 (8) (2011) 085409, pRB.
[42] S. Plimpton, Fast parallel algorithms for short-range molecular dynamics, J. Comput. Phys. 117 (1) (1995) 1–19, Available at <http://lammps.sandia.gov> (Version March 2015).
[43] S.Y. Kim, H.S. Park, On the effective plate thickness of monolayer graphene from flexural wave propagation, J. Appl. Phys. 110 (5) (2011) 054324.
[44] G. Zhang, B. Li, Thermal conductivity of nanotubes revisited: effects of chirality, isotope impurity, tube length, and temperature, J. Chem. Phys. 123 (11) (2005) 114714.
[45] C. Li, T.-W. Chou, Elastic wave velocities in single-walled carbon nanotubes, Phys. Rev. B 73 (24) (2006) 245407.
[46] J. Ford, The Fermi-Pasta-Ulam problem: paradox turns discovery, Phys. Rep. 213 (5) (1992) 271–310.
[47] G. Gallavotti, The Fermi-Pasta-Ulam Problem: A Status Report, vol. 728, Springer, 2007.
[48] J.-Y. Hsieh, J.-M. Lu, M.-Y. Huang, C.-C. Hwang, Theoretical variations in the Young's modulus of single-walled carbon nanotubes with tube radius and temperature: a molecular dynamics study, Nanotechnology 17 (15) (2006) 3920.
[49] A. Krishnan, E. Dujardin, T. Ebbesen, P. Yianilos, M. Treacy, Young's modulus of single-walled nanotubes, Phys. Rev. B 58 (20) (1998) 14013.
[50] R.C. Batra, S.S. Gupta, Wall thickness and radial breathing modes of single-walled carbon nanotubes, J. Appl. Mechs. – T ASME 75 (2008) 061010.
[51] S.S. Gupta, F. Bosco, R.C. Batra, Wall thickness and elastic moduli of single-walled carbon nanotubes from frequencies of axial, torsional and inextensional modes of vibration, Comput. Mater. Sci. 47 (2010) 1049–1059.
[52] A. Sears, R.C. Batra, Macroscopic properties of carbon nanotubes from molecular-mechanics simulations, Phys. Rev. B 69 (2004) 235406.